

Measurement of beam-recoil observables O_x , O_z and target asymmetry for the reaction $\gamma p \rightarrow K^+ \Lambda$

A. Lleres¹, O. Bartalini^{2,10}, V. Bellini^{13,6}, J.P. Bocquet¹, P. Calvat¹, M. Capogni^{2,10,4}, L. Casano¹⁰, M. Castoldi⁸, A. D'Angelo^{2,10}, J.-P. Didelez¹⁶, R. Di Salvo¹⁰, A. Fantini^{2,10}, D. Franco^{2,10}, C. Gaulard^{5,14}, G. Gervino^{3,11}, F. Ghio^{9,12}, B. Girolami^{9,12}, A. Giusa^{13,7}, M. Guidal¹⁶, E. Hourany¹⁶, R. Kunne¹⁶, V. Kuznetsov^{15,18}, A. Lapik¹⁵, P. Levi Sandri⁵, F. Mammoliti^{13,7}, G. Mandaglio^{7,17}, D. Moricciani¹⁰, A.N. Mushkarenkov¹⁵, V. Nedorezov¹⁵, L. Nicoletti^{2,10,1}, C. Perrin¹, C. Randieri^{13,6}, D. Rebreyend¹, F. Renard¹, N. Rudnev¹⁵, T. Russev¹, G. Russo^{13,7}, C. Schaerf^{2,10}, M.-L. Sperduto^{13,7}, M.-C. Sutura⁷, A. Turi¹⁵ (The GRAAL collaboration)

- ¹ LPSC, Université Joseph Fourier Grenoble 1, CNRS/IN2P3, Institut National Polytechnique de Grenoble, 53 avenue des Martyrs, 38026 Grenoble, France
- ² Dipartimento di Fisica, Università di Roma "Tor Vergata", via della Ricerca Scientifica 1, I-00133 Roma, Italy
- ³ Dipartimento di Fisica Sperimentale, Università di Torino, via P. Giuria, I-00125 Torino, Italy
- ⁴ Present affiliation: ENEA - C.R. Casaccia, via Anguillarese 301, I-00060 Roma, Italy
- ⁵ INFN - Laboratori Nazionali di Frascati, via E. Fermi 40, I-00044 Frascati, Italy
- ⁶ INFN - Laboratori Nazionali del Sud, via Santa Sofia 44, I-95123 Catania, Italy
- ⁷ INFN - Sezione di Catania, via Santa Sofia 64, I-95123 Catania, Italy
- ⁸ INFN - Sezione di Genova, via Dodecanneso 33, I-16146 Genova, Italy
- ⁹ INFN - Sezione di Roma, piazzale Aldo Moro 2, I-00185 Roma, Italy
- ¹⁰ INFN - Sezione di Roma Tor Vergata, via della Ricerca Scientifica 1, I-00133 Roma, Italy
- ¹¹ INFN - Sezione di Torino, I-10125 Torino, Italy
- ¹² Istituto Superiore di Sanità, viale Regina Elena 299, I-00161 Roma, Italy
- ¹³ Dipartimento di Fisica ed Astronomia, Università di Catania, via Santa Sofia 64, I-95123 Catania, Italy
- ¹⁴ Present affiliation: CSNSM, Université Paris-Sud 11, CNRS/IN2P3, 91405 Orsay, France
- ¹⁵ Institute for Nuclear Research, 117312 Moscow, Russia
- ¹⁶ IPNO, Université Paris-Sud 11, CNRS/IN2P3, 15 rue Georges Clémenceau, 91406 Orsay, France
- ¹⁷ Dipartimento di Fisica, Università di Messina, salita Sperone, I-98166 Messina, Italy
- ¹⁸ Kyungpook National University, 702-701, Daegu, Republic of Korea

Received: date / Revised version: date

Abstract. The double polarization (beam-recoil) observables O_x and O_z have been measured for the reaction $\gamma p \rightarrow K^+ \Lambda$ from threshold production to $E_\gamma \sim 1500$ MeV. The data were obtained with the linearly polarized beam of the GRAAL facility. Values for the target asymmetry T could also be extracted despite the use of an unpolarized target. Analyses of our results by two isobar models tend to confirm the necessity to include new or poorly known resonances in the 1900 MeV mass region.

PACS. 13.60.Le Meson production – 13.88.+e Polarization in interactions and scattering – 25.20.Lj Photoproduction reactions

1 Introduction

A detailed and precise knowledge of the nucleon spectroscopy is undoubtedly one of the cornerstones for our understanding of the strong interaction in the non-perturbative regime. Today's privileged way to get information on the excited states of the nucleon is light meson photo- and electroproduction. The corresponding database has considerably expanded over the last years thanks to a combined effort of a few dedicated facilities worldwide. Not only did the recent experiments brought a quantitative

improvement by measuring cross sections with unprecedented precision for a large number of channels but they also allowed a qualitative leap by providing for the first time high quality data on polarization observables. It is well known – and now well established – that these variables, being interference terms of various multipoles, bring unique and crucial constraints for partial wave analysis, hence facilitating the identification of resonant contributions and making parameter extraction more reliable.

From this perspective, $K^+ \Lambda$ photoproduction offers unique opportunities. Because the Λ is a self-analyzing particle, several polarization observables can be "easily"

measured via the analysis of its decay products. As a consequence, this reaction already possesses the richest database with results on the differential cross section [1]-[4], two single polarization observables (Σ and P) [2]-[6] and two double polarization observables (C_x and C_z) recently measured by the CLAS collaboration [7]. On the partial wave analysis side, the situation is particularly encouraging with most models concluding to the necessity of incorporating new or poorly known resonances to reproduce the full set of data. Some discrepancies do remain nonetheless either on the number of used resonances or on their identification. To lift the remaining ambiguities, new polarization observables are needed calling for new experiments.

In the present work, we report on first measurements of the beam-recoil observables O_x and O_z for the reaction $\gamma p \rightarrow K^+ \Lambda$ over large energy (from threshold to 1500 MeV) and angular ($\theta_{cm} = 30 - 140^\circ$) ranges. The target asymmetry T , indirectly extracted from the data, is also presented.

2 Experimental set-up

The experiment was carried-out with the GRAAL facility (see [8] for a detailed description), installed at the European Synchrotron Radiation Facility (ESRF) in Grenoble (France). The tagged and linearly polarized γ -ray beam is produced by Compton scattering of laser photons off the 6.03 GeV electrons circulating in the storage ring.

In the present experiment, we have used a set of UV lines at 333, 351 and 364 nm produced by an Ar laser, giving 1.40, 1.47 and 1.53 GeV γ -ray maximum energies, respectively. Some data were also taken with the green line at 514 nm (maximum energy of 1.1 GeV).

The photon energy is provided by an internal tagging system. The position of the scattered electron is measured by a silicon microstrip detector (128 strips with a pitch of 300 μm and 1000 μm thick). The measured energy resolution of 16 MeV is dominated by the energy dispersion of the electron beam (14 MeV - all resolutions are given as FWHM). The energy calibration is extracted run by run from the fit of the Compton edge position with a precision of $\sim 10 \mu\text{m}$, equivalent to $\Delta E_\gamma/E_\gamma \simeq 2 \times 10^{-4}$ (0.3 MeV at 1.5 GeV). A set of plastic scintillators used for time measurements is placed behind the microstrip detector. Thanks to a specially designed electronic module which synchronizes the detector signal with the RF of the machine, the resulting time resolution is ≈ 100 ps. The coincidence between detector signal and RF is used as a start for all Time-of-Flight (ToF) measurements and is part of the trigger of the experiment.

The energy dependence of the γ -ray beam polarization was determined from the Klein-Nishina formula taking into account the laser and electron beam emittances. The UV beam polarization is close to 100% at the maximum energy and decreases smoothly with energy to around 60% at the $K\Lambda$ threshold (911 MeV). Based on detailed studies [8], it was found that the only significant source of error

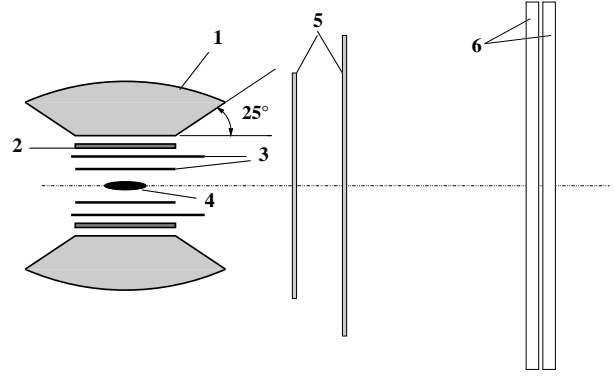


Fig. 1. Schematic view of the LA γ RANGE detector: BGO calorimeter (1), plastic scintillator barrel (2), cylindrical MWPCs (3), target (4), plane MWPCs (5), double plastic scintillator hodoscope (6) (the drawing is not to scale).

for the γ -ray polarization P_γ comes from the laser beam polarization ($\delta P_\gamma/P_\gamma = 2\%$).

A thin monitor is used to measure the beam flux (typically 10^6 γ /s). The monitor efficiency ($2.68 \pm 0.03\%$) was estimated by comparison with the response at low rate of a lead/scintillating fiber calorimeter.

The target cell consists of an aluminum hollow cylinder of 4 cm in diameter closed by thin mylar windows (100 μm) at both ends. Two different target lengths (6 and 12 cm) were used for the present experiment. The target was filled by liquid hydrogen at 18 K ($\rho \approx 7 \cdot 10^{-2}$ g/cm³).

The 4π LA γ RANGE detector of the GRAAL set-up allows to detect both neutral and charged particles (fig. 1). The apparatus is composed of two main parts: a central one ($25^\circ \leq \theta \leq 155^\circ$) and a forward one ($\theta \leq 25^\circ$).

The charged particle tracks are measured by a set of MultiWire Proportional Chambers (MWPC) (see [5] for a detailed description). To cover forward angles, two plane chambers, each composed of two planes of wires, are used. The detection efficiency of a track is about 95% and the average polar and azimuthal resolutions are 1.5° and 2° , respectively. The central region is covered by two coaxial cylindrical chambers. Single track efficiencies have been extracted for $\pi^0 p$ and $\pi^+ n$ reactions and were found to be $\geq 90\%$, in agreement with the simulation. Since this paper deals with polarization observables, no special study was done to assess the efficiency of multi track events. Angular resolutions were also estimated via simulation, giving 3.5° in θ and 4.5° in φ .

Charged particle identification in the central region is obtained by dE/dx technique thanks to a plastic scintillator barrel (32 bars, 5 mm thick, 43 cm long) with an energy resolution $\approx 20\%$. For the charged particles emitted in the forward direction, a Time-of-Flight measurement is provided by a double plastic scintillator hodoscope ($300 \times 300 \times 3$ cm³) placed at a distance of 3 m from the target and having a resolution of ≈ 600 ps. This detector provides also a measure of the energy loss dE/dx . Energy calibrations were extracted from the analysis of the $\pi^0 p$ photoproduction reaction while the ToF calibration of the

forward wall was obtained from fast electrons produced in the target.

Photons are detected in a BGO calorimeter made of 480 ($15\theta \times 32\varphi$) crystals, each of 21 radiation lengths. They are identified as clusters of adjacent crystals (3 on average for an energy threshold of 10 MeV per crystal) with no associated hit in the barrel. The measured energy resolution is 3% on average ($E_\gamma=200$ -1200 MeV). The angular resolution is 6° and 7° for polar and azimuthal angles, respectively ($E_\gamma \geq 200$ MeV and $l_{target}=3$ cm).

3 Data analysis

3.1 Channel selection

For the present results, the charged decay of the Λ ($\Lambda \rightarrow p\pi^-$, BR=63.9%) was considered and the same selection method used in our previous publication on $K\Lambda$ photo-production [5] was applied. Only the main points will be recalled in the following.

Only events with three tracks and no neutral cluster detected in the BGO calorimeter were retained. In the absence of a direct measurement of energy and/or momentum of the charged particles, the measured angles (θ , φ) of the three tracks were combined with kinematical constraints to calculate momenta. Particle identification was then obtained from the association of the calculated momenta with dE/dx and/or ToF measurements.

The main source of background is the $\gamma p \rightarrow p\pi^+\pi^-$ reaction, a channel with a similar final state and a cross section hundred times larger. Selection of the $K\Lambda$ final state was achieved by applying narrow cuts on the following set of experimental quantities:

- . Energy balance.
- . Effective masses of the three particles extracted from the combination of measured dE/dx and ToF (only at forward angles) with calculated momenta.
- . Missing mass $m_{\gamma p \rightarrow K^+}$ evaluated from E_γ , θ_K (measured) and p_K (calculated).

For each of these variables, the width σ of the corresponding distribution (Gaussian-like shape) were extracted from a Monte-Carlo simulation of the apparatus response based on the GEANT3 package of the CERN library.

To check the quality of the event selection, the distribution of the Λ decay length was used due to its high sensitivity to background contamination.

Event by event, track information and Λ momentum were combined to obtain the distance d between the reaction and decay vertices. The Λ decay length was then calculated with the usual formula $ct_\Lambda = d/(\beta_\Lambda * \gamma_\Lambda)$. Fig. 2 shows the resulting distributions for events selected with all cuts at $\pm 2\sigma$ (closed circles) compared with events without cuts (open circles). These spectra were corrected for detection efficiency losses estimated from the Monte-Carlo simulation (significant only for $ct \geq 5$ cm). It should be

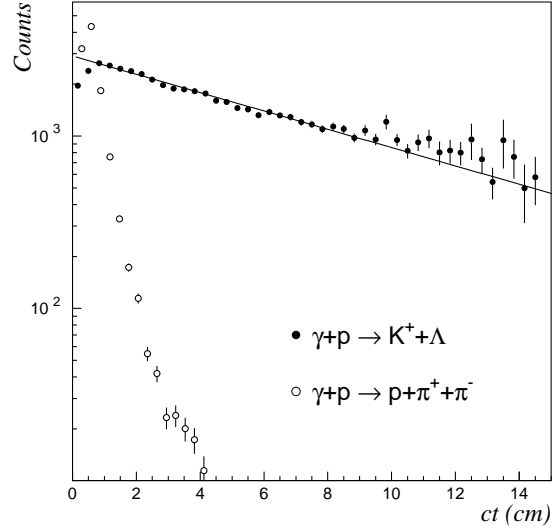


Fig. 2. Reconstructed Λ decay length spectrum after all selection cuts (closed circles) for events with at least two tracks in the cylindrical chambers. The solid line represents the fit with an exponential function $\alpha * \exp(-ct/c\tau)$ where α and $c\tau$ are free parameters. The second distribution (open circles) was obtained without applying selection cuts. It corresponds to the main background reaction ($\gamma p \rightarrow p\pi^+\pi^-$) which, as expected, contributes only to small ct values.

noted that the deficit in the first bins is attributed to finite resolution effects not fully taken into account in the simulation.

The first spectrum was fitted for $ct \geq 1$ cm by an exponential function $\alpha * \exp(-ct/c\tau)$ with α and $c\tau$ as free parameters. The fitted $c\tau$ value (8.17 ± 0.31 cm) is in good agreement with the PDG expectation for the Λ mean free path ($c\tau_\Lambda = 7.89$ cm) [9].

By contrast, the spectrum without cuts is dominated by $p\pi^+\pi^-$ background events. As expected, they contribute mostly to small ct values (≤ 2 -3 cm), making the shape of this distribution highly sensitive to background contamination. For instance, a pronounced peak already shows up when opening selection cuts at $\pm 3\sigma$.

A remaining source of background, which cannot be seen in the ct plot presented above, originates from the contamination by the reaction $\gamma p \rightarrow K^+ \Sigma^0$. Indeed, events where the decay photon is not detected are retained by the first selection step. Since these events are kinematically analyzed as $K\Lambda$ ones, most of them are nevertheless rejected by the selection cuts. From the simulation, this contamination was found to be of the order of 2%.

As a further check of the quality of the data sample, the missing mass spectrum was calculated. One should remember that the missing mass is not directly measured and is not used as a criterion for the channel identification. The spectrum presented in fig. 3 (closed circles) is in fair agreement with the simulated distribution (solid line). Some slight discrepancies can nevertheless be seen

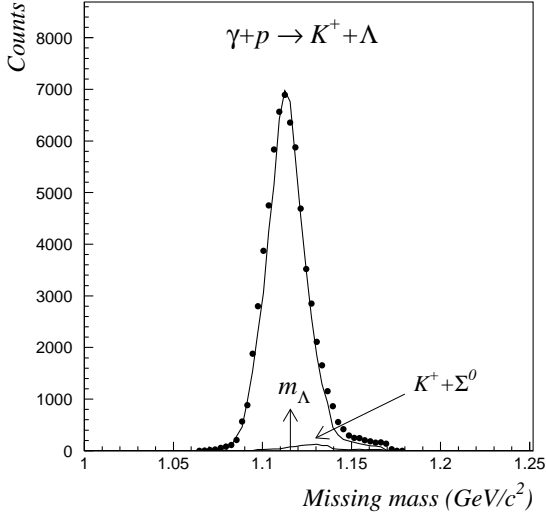


Fig. 3. Distribution of the missing mass $m_{\gamma p \rightarrow K^+ \Lambda}$ reconstructed from measured E_γ and θ_K and calculated p_K . Data after all selection cuts (closed circles) are compared to the simulation (solid line). The expected contribution from the reaction $\gamma p \rightarrow K^+ \Sigma^0$ is also plotted (note that it is not centered on the Σ^0 mass due to kinematical constraints in the event analysis). The vertical arrow indicates the Λ mass.

in the high energy tail of the spectra. The simulated missing mass distribution of the contamination from the $\gamma p \rightarrow K^+ \Sigma^0$ reaction, also displayed in fig. 3, clearly indicates that such a background cannot account for the observed differences. Rather, these are attributed to the summation of a large number of data taking periods with various experimental configurations (target length, wire chambers, green vs UV laser line, ...). Although these configurations were implemented in corresponding simulations, small imperfections (misalignments in particular) could not be taken into account.

To summarize, thanks to these experimental checks, we are confident that the level of background in our selected sample is limited. This is corroborated by the simulation from which the estimated background contamination (multi-pions and $K^+ \Sigma^0$ contributions) never exceeds 5% whatever the incident photon energy or the meson recoil angle.

3.2 Measurement of O_x , O_z and T

As will be shown below, the beam-recoil observables O_x and O_z , as well as the target asymmetry T , can be extracted from the angular distribution of the Λ decay proton.

3.2.1 Formalism

For a linearly polarized beam and an unpolarized target, the differential cross section can be expressed in terms of the single polarization observables Σ , P , T (beam asymmetry, recoil polarization, target asymmetry, respectively) and of the double polarization observables O_x , O_z (beam-recoil), as follows [10]:

$$\begin{aligned} \rho_f \frac{d\sigma}{d\Omega} = \frac{1}{2} \left(\frac{d\sigma}{d\Omega} \right)_0 & [1 - P_\gamma \Sigma \cos 2\varphi_\gamma \\ & + \sigma_{x'} P_\gamma O_x \sin 2\varphi_\gamma \\ & + \sigma_{y'} (P - P_\gamma T \cos 2\varphi_\gamma) \\ & + \sigma_{z'} P_\gamma O_z \sin 2\varphi_\gamma] \end{aligned} \quad (1)$$

ρ_f is the density matrix for the lambda final state and $(d\sigma/d\Omega)_0$ the unpolarized differential cross section. The Pauli matrices $\sigma_{x',y',z'}$ refer to the lambda quantization axes defined by \hat{z}' along the lambda momentum in the center-of-mass frame and \hat{y}' perpendicular to the reaction plane (fig. 4). P_γ is the degree of linear polarization of the beam along an axis defined by $\hat{n} = \hat{x} \cos \varphi_\gamma + \hat{y} \sin \varphi_\gamma$; the photon quantization axes are defined by \hat{z} along the proton center-of-mass momentum and $\hat{y} = \hat{y}'$ (fig. 4). We have $\varphi_\gamma = \varphi_{lab} - \varphi$, where φ_{lab} and φ are the azimuthal angles of the photon polarization vector and of the reaction plane in the laboratory axes, respectively (fig. 5).

The beam-recoil observables C_x and C_z measured by the CLAS collaboration with a circularly polarized beam [7] were obtained using another coordinate system for describing the hyperon polarization, the \hat{z}' axis being along the incident beam direction instead of the momentum of one of the recoiling particles (see fig. 4). Such a non-standard coordinate system was chosen to give the results their simplest interpretation in terms of polarization transfer but implied the model calculations to be adapted. To check the consistency of our results with the CLAS values (see sect. 4.1), our O_x and O_z values were converted using the following rotation matrix:

$$\begin{aligned} O_x^c &= -O_x \cos \theta_{cm} - O_z \sin \theta_{cm} \\ O_z^c &= O_x \sin \theta_{cm} - O_z \cos \theta_{cm} \end{aligned} \quad (2)$$

It should be noted that our definition for O_x and O_z (eq. 1) has opposite sign with respect to the definition given in the article [11], which is used in several hadronic models. We chose the same sign convention than the CLAS collaboration.

For an outgoing lambda with an arbitrary quantization axis \hat{n}' , the differential cross section becomes:

$$\mathbf{P}_\Lambda \cdot \hat{n}' \frac{d\sigma}{d\Omega} = \text{Tr} \left[\sigma \cdot \hat{n}' \rho_f \frac{d\sigma}{d\Omega} \right] \quad (3)$$

where \mathbf{P}_Λ is the polarization vector of the lambda. If the polarization is not observed, the expression for the differential cross section reduces to:

$$\frac{d\sigma}{d\Omega} = \text{Tr} \left[\rho_f \frac{d\sigma}{d\Omega} \right] \quad (4)$$

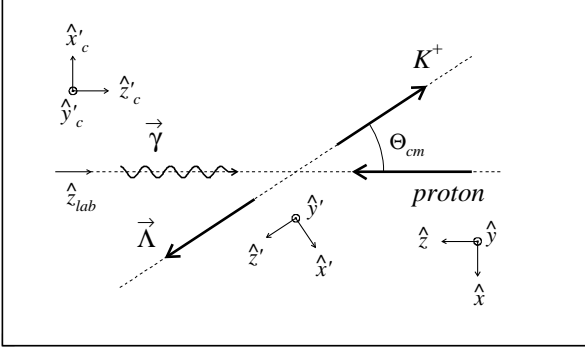


Fig. 4. Definition of the coordinate systems and polar angles in the center-of-mass frame (viewed in the reaction plane). The $[\hat{x}', \hat{y}', \hat{z}']$ system is used to specify the polarization of the outgoing Λ baryon: \hat{z}' is along the Λ momentum and \hat{y}' perpendicular to the reaction plane. The $[\hat{x}, \hat{y}, \hat{z}]$ system is used to specify the incident photon polarization: \hat{z} is along the incoming proton momentum and \hat{y} identical to \hat{y}' . The polar angle θ_{cm} of the outgoing K^+ meson is defined with respect to the incident beam direction \hat{z}_{lab} . $[\hat{x}'_c, \hat{y}'_c, \hat{z}'_c]$ is the coordinate system chosen by the CLAS collaboration for the Λ polarization. The \hat{x}'_c and \hat{z}'_c axes are obtained from \hat{x}' and \hat{z}' by a rotation of angle $\pi + \theta_{cm}$.

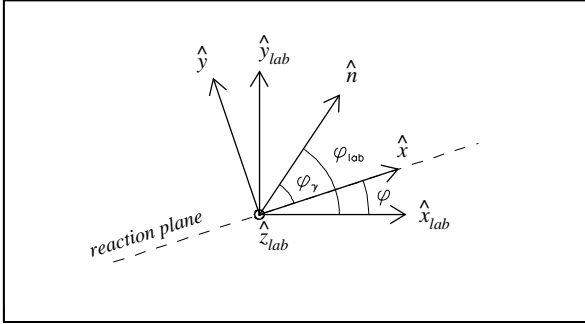


Fig. 5. Definition of the coordinate systems and azimuthal angles in the center-of-mass frame (viewed perpendicularly to the beam direction). The $[\hat{x}_{lab}, \hat{y}_{lab}, \hat{z}_{lab}]$ system corresponds to the laboratory axes with \hat{z}_{lab} along the incident beam direction. The $[\hat{x}, \hat{y}, \hat{z}]$ system, used to define the incident photon polarization, has its axes \hat{x} and \hat{y} along and perpendicular to the reaction plane (azimuthal angle φ), respectively. The polarization of the beam is along \hat{n} (azimuthal angle φ_{lab}). The two beam polarization states correspond to $\varphi_{lab} = 0^0$ (horizontal) and $\varphi_{lab} = 90^0$ (vertical) ($\varphi_{lab} = \varphi_\gamma + \varphi$).

which leads to:

$$\frac{d\sigma}{d\Omega} = \left(\frac{d\sigma}{d\Omega} \right)_0 [1 - P_\gamma \Sigma \cos 2\varphi_\gamma] \quad (5)$$

For horizontal ($\varphi_{lab} = 0^0$) and vertical ($\varphi_{lab} = 90^0$) photon polarizations, the corresponding azimuthal distributions of the reaction plane are therefore:

$$\frac{d\sigma}{d\Omega}(\varphi_{lab} = 0^0) = \left(\frac{d\sigma}{d\Omega} \right)_0 [1 - P_\gamma \Sigma \cos 2\varphi] \quad (6)$$

$$\frac{d\sigma}{d\Omega}(\varphi_{lab} = 90^0) = \left(\frac{d\sigma}{d\Omega} \right)_0 [1 + P_\gamma \Sigma \cos 2\varphi] \quad (7)$$

The beam asymmetry values Σ published in [5] were extracted from the fit of the azimuthal distributions of the ratio:

$$\frac{N(\varphi_{lab} = 90^0) - N(\varphi_{lab} = 0^0)}{N(\varphi_{lab} = 90^0) + N(\varphi_{lab} = 0^0)} = P_\gamma \Sigma \cos 2\varphi \quad (8)$$

3.2.2 Λ polarization and spin observables

The components of the lambda polarization vector deduced from eqs. 1 to 5 are:

$$P_\Lambda^{x', z'} = \frac{P_\gamma O_{x,z} \sin 2\varphi_\gamma}{1 - P_\gamma \Sigma \cos 2\varphi_\gamma} \quad (9)$$

$$P_\Lambda^{y'} = \frac{P - P_\gamma T \cos 2\varphi_\gamma}{1 - P_\gamma \Sigma \cos 2\varphi_\gamma} \quad (10)$$

These equations provide the connection between the Λ polarisation \mathbf{P}_Λ and the spin observables Σ , P , T , O_x and O_z .

Integration of the polarization components over the azimuthal angle φ of the reaction plane writes:

$$\langle P_\Lambda^i \rangle = \frac{\int P_\Lambda^i(\varphi) \frac{d\sigma}{d\Omega}(\varphi) d\varphi}{\int \frac{d\sigma}{d\Omega}(\varphi) d\varphi} \quad (11)$$

where i stands for x' , y' or z' .

When integrating over the full angular domain, the averaged x' and z' components of the polarization vector vanish while the y' component is equal to P . On the other hand, when integrating over appropriately chosen angular sectors, all three averaged components can remain different from zero. For horizontal and vertical beam polarizations, the following expressions are obtained when considering the four particular φ domains defined hereafter [12] (recalling $\varphi_\gamma = \varphi_{lab} - \varphi$):

- $S_1 = [\pi/4, 3\pi/4] \cup [5\pi/4, 7\pi/4]$:
 $\langle P_\Lambda^{y'} \rangle (\varphi_{lab} = 0^0) = (P\pi + 2P_\gamma T)/(\pi + 2P_\gamma \Sigma)$
 $\langle P_\Lambda^{y'} \rangle (\varphi_{lab} = 90^0) = (P\pi - 2P_\gamma T)/(\pi - 2P_\gamma \Sigma)$
- $S_2 = [-\pi/4, \pi/4] \cup [3\pi/4, 5\pi/4]$:
 $\langle P_\Lambda^{y'} \rangle (\varphi_{lab} = 0^0) = (P\pi - 2P_\gamma T)/(\pi - 2P_\gamma \Sigma)$
 $\langle P_\Lambda^{y'} \rangle (\varphi_{lab} = 90^0) = (P\pi + 2P_\gamma T)/(\pi + 2P_\gamma \Sigma)$
- $S_3 = [0, \pi/2] \cup [\pi, 3\pi/2]$:
 $\langle P_\Lambda^{x', z'} \rangle (\varphi_{lab} = 0^0) = -2P_\gamma O_{x,z}/\pi$
 $\langle P_\Lambda^{x', z'} \rangle (\varphi_{lab} = 90^0) = +2P_\gamma O_{x,z}/\pi$
- $S_4 = [\pi/2, \pi] \cup [3\pi/2, 2\pi]$:
 $\langle P_\Lambda^{x', z'} \rangle (\varphi_{lab} = 0^0) = +2P_\gamma O_{x,z}/\pi$
 $\langle P_\Lambda^{x', z'} \rangle (\varphi_{lab} = 90^0) = -2P_\gamma O_{x,z}/\pi$

It should be noted that these four sectors cover the full φ range. In the following, these different combinations of φ sectors and polarization states will be labelled by the sign plus or minus appearing in the corresponding expressions for $\langle P_A^i \rangle$.

3.2.3 Decay angular distribution

In the lambda rest frame, the angular distribution of the decay proton is given by [13]:

$$W(\cos \theta_p) = \frac{1}{2}(1 + \alpha |\mathbf{P}_A| \cos \theta_p) \quad (12)$$

where $\alpha=0.642\pm 0.013$ [9] is the Λ decay parameter and θ_p the angle between the proton direction and the lambda polarization vector.

From this expression, one can derived an angular distribution for each component of \mathbf{P}_A :

$$W(\cos \theta_p^i) = \frac{1}{2}(1 + \alpha P_A^i \cos \theta_p^i) \quad (13)$$

where θ_p^i is now the angle between the proton direction and the quantization axis i (x' , y' or z').

The components being determined in the Λ rest frame, a suitable transformation should be applied to calculate them in the center-of-mass frame. However, as the boost direction is along the lambda momentum, it can be shown that the polarization measured in the lambda rest frame remains unchanged in the center-of-mass frame [7].

When integrating over all possible azimuthal angles φ , the proton angular distribution with respect to the y' -axis simply writes:

$$W(\cos \theta_p^{y'}) = \frac{1}{2}(1 + \alpha P \cos \theta_p^{y'}) \quad (14)$$

where P is the recoil polarization. Our P results published in [5] were determined directly from the measured up/down asymmetry:

$$\frac{N(\cos \theta_p^{y'} > 0) - N(\cos \theta_p^{y'} < 0)}{N(\cos \theta_p^{y'} > 0) + N(\cos \theta_p^{y'} < 0)} = \frac{1}{2}\alpha P \quad (15)$$

When integrating over the different angular domains specified above (sectors $S_1 + S_2$ for y' -axis and $S_3 + S_4$ for x' -, z' -axes, appropriately combined with the two beam polarization), the proton angular distributions with respect to the three quantization axes can be written as follows:

$$W_{\pm}(\cos \theta_p^{x',z'}) = \frac{1}{2}(1 \pm \alpha \frac{2P_{\gamma} O_{x,z}}{\pi} \cos \theta_p^{x',z'}) \quad (16)$$

$$W_{\pm}(\cos \theta_p^{y'}) = \frac{1}{2}(1 + \alpha \frac{P\pi \pm 2P_{\gamma}T}{\pi \pm 2P_{\gamma}\Sigma} \cos \theta_p^{y'}) \quad (17)$$

3.2.4 Experimental extraction

As for Σ and P , the observables O_x , O_z and T were extracted from ratios of the angular distributions, in order to get rid of most of the distortions introduced by the experimental acceptance.

Including the detection efficiencies, the yields measured as a function of the proton angle with respect to the different axes write:

$$N_{\pm}^{x',z'} = \frac{1}{2}N_{0\pm}^{x',z'} \epsilon_{\pm}(\cos \theta_p^{x',z'}) (1 \pm \alpha \frac{2P_{\gamma} O_{x,z}}{\pi} \cos \theta_p^{x',z'}) \quad (18)$$

$$N_{\pm}^{y'} = \frac{1}{2}N_{0\pm}^{y'} \epsilon_{\pm}(\cos \theta_p^{y'}) (1 + \alpha \frac{P\pi \pm 2P_{\gamma}T}{\pi \pm 2P_{\gamma}\Sigma} \cos \theta_p^{y'}) \quad (19)$$

From the integration of the azimuthal distributions given by eqs. 6 and 7 over the different angular sectors, it can be shown that:

$$N_{0+}^{x',z'} = N_{0-}^{x',z'} \quad (20)$$

$$\frac{N_{0+}^{y'}}{N_{0-}^{y'}} = \frac{\pi + 2P_{\gamma}\Sigma}{\pi - 2P_{\gamma}\Sigma} \quad (21)$$

Assuming that the detection efficiencies do not depend on the considered φ sectors ($\epsilon_{+}(\cos \theta_p^i) = \epsilon_{-}(\cos \theta_p^i)$ - the validity of this assumption will be discussed later on), we can then calculate the following sums and ratios from which the efficiency cancels out:

$$N_{+}^{x',z'} + N_{-}^{x',z'} = \frac{1}{2}(N_{0+}^{x',z'} + N_{0-}^{x',z'}) \epsilon_{\pm}(\cos \theta_p^{x',z'}) \quad (22)$$

$$N_{+}^{y'} + N_{-}^{y'} = \frac{1}{2}(N_{0+}^{y'} + N_{0-}^{y'}) \epsilon_{\pm}(\cos \theta_p^{y'}) (1 + \alpha P \cos \theta_p^{y'}) \quad (23)$$

$$\frac{2N_{+}^{x',z'}}{N_{+}^{x',z'} + N_{-}^{x',z'}} = (1 + \alpha \frac{2P_{\gamma} O_{x,z}}{\pi} \cos \theta_p^{x',z'}) \quad (24)$$

$$\frac{2N_{+}^{y'}}{N_{+}^{y'} + N_{-}^{y'}} = (1 + \frac{2P_{\gamma}\Sigma}{\pi}) (\frac{1 + \alpha \frac{P\pi + 2P_{\gamma}T}{\pi + 2P_{\gamma}\Sigma} \cos \theta_p^{y'}}{1 + \alpha P \cos \theta_p^{y'}}) \quad (25)$$

To illustrate the extraction method of O_x , O_z and T , the N_{+} and N_{-} experimental distributions together with their sums and ratios, summed over all photon energies and meson polar angles, are displayed in figs. 6 (x' -axis), 7 (z' -axis) and 8 (y' -axis). Thanks to the efficiency correction given by the distributions $N_{+} + N_{-}$ (figs. 6,7,8-c), the ratios $2N_{+}/(N_{+} + N_{-})$ (figs. 6,7,8-d), from which the efficiency drops out, exhibit the expected dependence in $\cos \theta_p$ and can be therefore fitted by the functions given in

the r.h.s. of eqs. 24 and 25. The known energy dependence of P_γ and the previously measured values for Σ and P [5] are then used to deduce O_x , O_z and T from the fitted slopes.

The validity of the hypothesis $\epsilon_+(\cos\theta_p^i) = \epsilon_-(\cos\theta_p^i)$ was studied via the Monte Carlo simulation in which a polarized Λ decay was included. The efficiencies ϵ_\pm calculated from the simulation are presented in plots e) of figs. 6 to 8 and the ratios ϵ_-/ϵ_+ in plots f) (open circles). As one can see, for the y' case, this ratio remains very close to 1 whatever the angle while, for x' and z' , the discrepancy from 1 is more pronounced and evolves with the angle. This shows that some corrections should be applied on the measured ratios $2N_+/(N_+ + N_-)$ to take into account the non-negligible differences observed between ϵ_+ and ϵ_- . The correction factors, plotted in figs. 6,7,8-f) (closed circles), were calculated through the following expression:

$$Cor = \left(\frac{2N_+^i}{N_+^i + N_-^i}\right)_{gen} / \left(\frac{2N_+^i}{N_+^i + N_-^i}\right)_{sel} \quad (26)$$

where *gen* and *sel* stand for generated and selected events. Since $\epsilon_\pm = (N_\pm)_{sel}/(N_\pm)_{gen}$, it can be re-written as:

$$Cor = \frac{1}{2} \left(\frac{2N_+^i}{N_+^i + N_-^i}\right)_{gen} \left[1 + \frac{\epsilon_-^i}{\epsilon_+^i} \left(\frac{N_-^i}{N_+^i}\right)_{gen}\right] \quad (27)$$

The corrected distributions are displayed in the plots g) of figs. 6 to 8. After correction, as expected, the slope of the y' distribution is unaffected while the slopes of the x' and z' distributions are slightly modified. These distributions were again fitted to obtain the final values of O_x , O_z and T .

As the detection efficiencies and the correction factors calculated from the simulation depend on the input values of O_x , O_z and T , an iterative method was used. Three iterations were sufficient to reach stable values.

For a consistency check, an alternative extraction method was implemented. The angular distributions were directly corrected by the simulated efficiencies and fitted according to:

$$\frac{N_+^{x',z'} + N_-^{x',z',inv}}{\epsilon_+^{x',z'} + \epsilon_-^{x',z',inv}} = \frac{1}{2} N_{0+}^{x',z'} \left(1 + \alpha \frac{2P_\gamma O_{x,z}}{\pi} \cos\theta_p^{x',z'}\right) \quad (28)$$

$$\frac{N_+^{y'}}{\epsilon_+^{y'}} = \frac{1}{2} N_{0+}^{y'} \left(1 + \alpha \frac{P\pi + 2P_\gamma T}{\pi + 2P_\gamma \Sigma} \cos\theta_p^{y'}\right) \quad (29)$$

$$\frac{N_-^{y'}}{\epsilon_-^{y'}} = \frac{1}{2} N_{0+}^{y'} \frac{\pi - 2P_\gamma \Sigma}{\pi + 2P_\gamma \Sigma} \left(1 + \alpha \frac{P\pi - 2P_\gamma T}{\pi - 2P_\gamma \Sigma} \cos\theta_p^{y'}\right) \quad (30)$$

where N^{inv} and ϵ^{inv} stand for $N(-\cos\theta_p)$ and $\epsilon(-\cos\theta_p)$, respectively. This trick, used for the x' and z' cases, allows to combine the N_+ and N_- distributions which have opposite slopes (eq. 18).

To illustrate this second extraction method, the corrected distributions, summed over all photon energies and meson polar angles, are displayed in figs. 6,7-j) (x' , z' -axes) and 8-h),i) (y' -axis). They were obtained by dividing the originally measured distributions (figs. 6,7-h and 8-a,b) by the corresponding efficiency distributions (figs. 6,7-i and 8-e). In the y' -axis case, the two corrected spectra N_\pm/ϵ_\pm were simultaneously fitted.

This method gives results in good agreement with those extracted from the first method. Nevertheless, the resulting χ^2 were found to be significantly larger (the global reduced- χ^2 values are given in figs. 6 to 8 - they are close to 1 for the first method and five to ten times larger for the second one). The first method, which relies upon ratios leading to an intrinsic first order efficiency correction, is less dependent on the simulation details and was therefore preferred.

Three sources of systematic errors were taken into account: the laser beam polarization ($\delta P_\gamma/P_\gamma=2\%$), the Λ decay parameter α ($\delta\alpha = 0.013$) and the hadronic background. The error due to the hadronic background was estimated from the variation of the extracted values when cuts were changed from $\pm 2\sigma$ to $\pm 2.5\sigma$. Given the good agreement between the two extraction methods, no corresponding systematic error was considered. For the T observable, the measured values for Σ and P being involved, their respective errors were included in the estimation of the uncertainty. All systematic and statistical errors have been summed quadratically.

4 Results and discussions

The complete set of beam-recoil polarization and target asymmetry data is displayed in figs. 9 to 15. These data cover the production threshold region ($E_\gamma=911-1500$ MeV) and a large angular range ($\theta_{cm}^{kaon} = 30 - 140^\circ$). Numerical values are listed in tables 1 to 3. Error bars are the quadratic sum of statistical and systematic errors.

4.1 Observable combination and consistency check

In pseudoscalar meson photoproduction, one can extract experimentally 16 different quantities: the unpolarized differential cross section $(d\sigma/d\Omega)_0$, 3 single polarization observables (P , T , Σ), 4 beam-target polarizations (E , F , G , H), 4 beam-recoil polarizations (C_x , C_z , O_x , O_z) and 4 target-recoil polarizations (T_x , T_z , L_x , L_z). The various spin observables are not independent but are constrained by non-linear identities and various inequalities [10], [11], [14], [15]. In particular, of the seven single and beam-recoil polarization observables, only five are independent being related by the two equations:

$$C_x^2 + C_z^2 + O_x^2 + O_z^2 = 1 + T^2 - P^2 - \Sigma^2 \quad (31)$$

$$C_z O_x - C_x O_z = T - P \Sigma \quad (32)$$

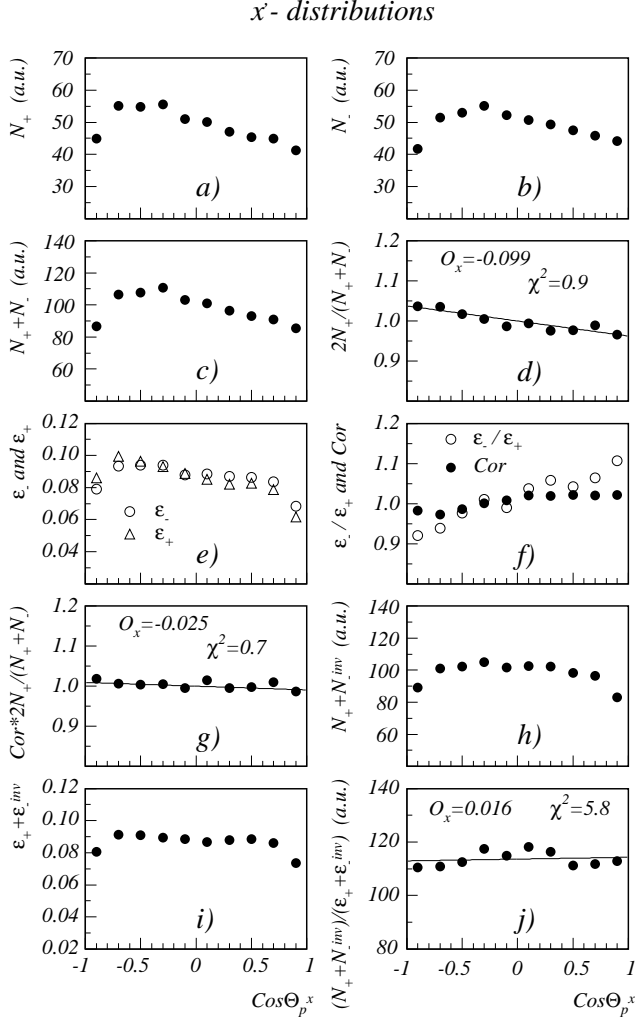


Fig. 6. Angular distributions for the decay proton in the lambda rest frame with respect to the x' -axis: a) distribution N_+ ; b) distribution N_- ; c) sum $N_+ + N_-$; d) ratio $2N_+/(N_+ + N_-)$; e) efficiencies ϵ_+ (triangles) and ϵ_- (circles) calculated from the simulation; f) ratio ϵ_-/ϵ_+ and correction factor Cor (closed circles) given by eq. 26 calculated from the simulation; g) ratio $2N_+/(N_+ + N_-)$ corrected by the factor Cor ; h) distribution $N_+ + N_-^{inv}$, with $N_-^{inv} = N(-\cos\theta_p)$; i) efficiency $\epsilon_+ + \epsilon_-^{inv}$, with $\epsilon_-^{inv} = \epsilon(-\cos\theta_p)$, calculated from the simulation; j) distribution $N_+ + N_-^{inv}$ corrected by the efficiency $\epsilon_+ + \epsilon_-^{inv}$. The solid line in d) and g) represents the fit by the (linear) function given in the r.h.s. of eq. 24. The solid line in j) represents the fit by the (linear) function given in the r.h.s. of eq. 28. The reduced- χ^2 and the O_x value obtained from the fits are reported in d), g) and j).

There are also a number of inequalities involving three of these observables:

$$|T \pm P| \leq 1 \pm \Sigma \quad (33)$$

$$P^2 + O_x^2 + O_z^2 \leq 1 \quad (34)$$

$$\Sigma^2 + O_x^2 + O_z^2 \leq 1 \quad (35)$$

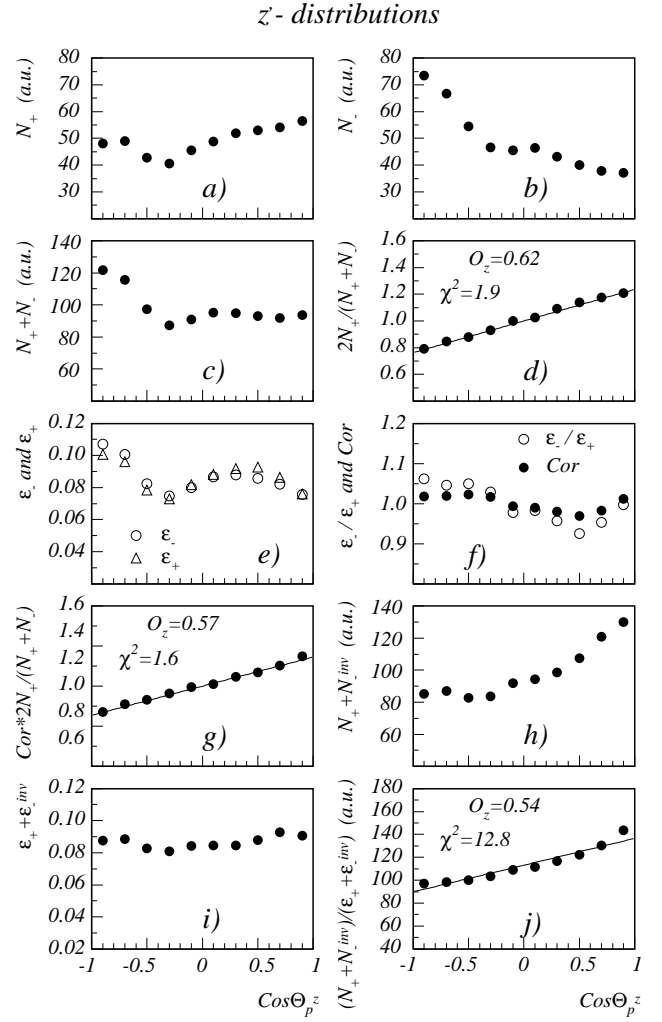


Fig. 7. Angular distributions for the decay proton in the lambda rest frame with respect to the z' -axis (all distributions as in fig. 6). The reduced- χ^2 and the O_z value obtained from the fits are reported in d), g) and j).

$$P^2 + C_x^2 + C_z^2 \leq 1 \quad (36)$$

$$\Sigma^2 + C_x^2 + C_z^2 \leq 1 \quad (37)$$

These different identities and inequalities can be used to test the consistency of our present and previous measurements. They can also be used to check the compatibility of our data with the results on C_x and C_z recently published by the CLAS collaboration [7].

Our measured values for Σ , P , T , O_x and O_z were combined to test the above inequalities. Equation 31 was used to calculate the quantity $C_x^2 + C_z^2$ appearing in expressions 36 and 37. The results for the two combinations $|T \pm P| \mp \Sigma$ of the three single polarizations are presented in fig. 12. The results for the quantities:

$$\begin{aligned} & \cdot (P^2 + O_x^2 + O_z^2)^{1/2}, \\ & \cdot (\Sigma^2 + O_x^2 + O_z^2)^{1/2}, \end{aligned}$$

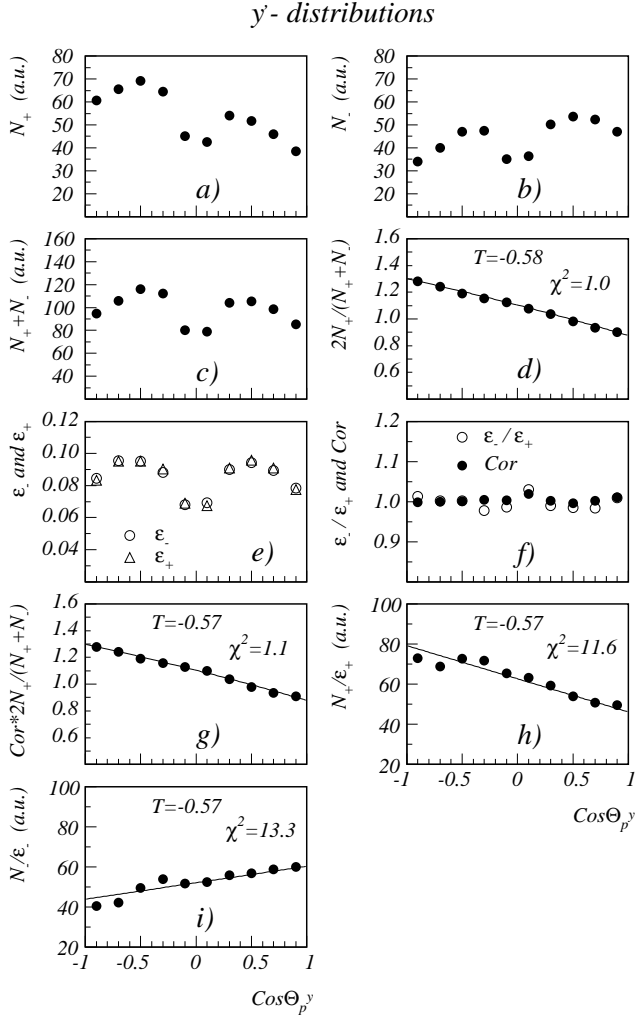


Fig. 8. Angular distributions for the decay proton in the lambda rest frame with respect to the y' -axis: a) distribution N_+ ; b) distribution N_- ; c) sum $N_+ + N_-$; d) ratio $2N_+/(N_+ + N_-)$; e) efficiencies ϵ_+ (triangles) and ϵ_- (circles) calculated from the simulation - they are symmetrical about $\theta_{cm} = 90^\circ$ (we find $\epsilon_{down}/\epsilon_{up}=1.03$); f) ratio ϵ_-/ϵ_+ (open circles) and correction factor Cor (closed circles) given by eq. 26 calculated from the simulation; g) ratio $2N_+/(N_+ + N_-)$ corrected by the factor Cor ; h) distribution N_+ corrected by the efficiency ϵ_+ ; i) distribution N_- corrected by the efficiency ϵ_- . The solid line in d) and g) represents the fit by the (non-linear) function given in the r.h.s. of eq. 25. These distributions exhibit a linear behaviour since the overall recoil polarisation P is very low (the value extracted from the up/down asymmetry of the raw distribution $N_+ + N_-$ is -0.12). The solid line in h) and i) represents the simultaneous fit by the (linear) functions given in the r.h.s. of eqs. 29 and 30. The reduced- χ^2 and the T value obtained from the fits are reported in d), g), h) and i).

$$\begin{aligned} \cdot (1 + T^2 - P^2 - O_x^2 - O_z^2)^{1/2} &= (\Sigma^2 + C_x^2 + C_z^2)^{1/2}, \\ \cdot (1 + T^2 - \Sigma^2 - O_x^2 - O_z^2)^{1/2} &= (P^2 + C_x^2 + C_z^2)^{1/2}, \end{aligned}$$

which combine single and double polarization observables, are displayed in figs. 13 and 14. All these quantities should be ≤ 1 . The plotted uncertainties are given by the standard error propagation. Whatever the photon energy or the meson polar angle, no violation of the expected inequalities is observed, confirming the internal consistency of our set of data.

Since all observables entering in eqs. 31 and 32 were measured either by GRAAL (Σ , P , T , O_x , O_z) or by CLAS (P , C_x , C_z - their P data were confirmed by our measurements [5]), the two sets of data can be therefore compared and combined. Within the error bars, the agreement between the two sets of equal combinations $(1+T^2-\Sigma^2-O_x^2-O_z^2)^{1/2}$ (GRAAL) and $(P^2+C_x^2+C_z^2)^{1/2}$ (CLAS) is fair (fig. 14) and tends to confirm the previously observed saturation to the value 1 of $R = (P^2 + C_x^2 + C_z^2)^{1/2}$, whatever the energy or angle. Fig. 15 displays the values for the combined GRAAL-CLAS quantity $C_z O_x - C_x O_z - T + P \Sigma$. Within the uncertainties, the expected value (1) is obtained, confirming again the overall consistency of the GRAAL and CLAS data.

It has been demonstrated [14] that the knowledge of the unpolarized cross section, the three single-spin observables and at least four double-spin observables - provided they have not all the same type - is sufficient to determine uniquely the four complex reaction amplitudes. Therefore, only one additional double polarization observable measured using a polarized target will suffice to extract unambiguously these amplitudes.

4.2 Comparison to models

We have compared our results with two models: the Ghent isobar RPR (Regge-plus-resonance) model [16]-[19] and the coupled-channel partial wave analysis developed by the Bonn-Gatchina collaboration [20]-[24]. In the following, these models will be referred as RPR and BG, respectively. The comparison is shown in figs. 9 to 11.

The RPR model is an isobar model for $K\Lambda$ photo- and electroproduction. In addition to the Born and kaonic contributions, it includes a Reggeized t-channel background which is fixed to high-energy data. The fitted database includes differential cross section, beam asymmetry and recoil polarization photoproduction results. The model variant presented here contains, besides the known N^* resonances ($S_{11}(1650)$, $P_{11}(1710)$, $P_{13}(1720)$), the $P_{13}(1900)$ state (** in the PDG [9]) and a missing $D_{13}(1900)$ resonance. This solution was found to provide the best overall agreement with the combined photo- and electroproduction database. As one can see in figs. 9 to 11, the RPR prediction (dashed line) qualitatively reproduces all observed structures. Interestingly enough, the model best reproduces the data at high energy (1400-1500 MeV), where the $P_{13}(1900)$ and $D_{13}(1900)$ contributions are maximal.

The BG model is a combined analysis of experiments with πN , ηN , $K\Lambda$ and $K\Sigma$ final states. As compared

to the other models, this partial-wave analysis takes into account a much larger database which includes most of the available results (differential cross sections and polarization observables). For the $\gamma p \rightarrow K^+ \Lambda$ reaction, the main resonant contributions come from the $S_{11}(1535)$, $S_{11}(1650)$, $P_{13}(1720)$, $P_{13}(1900)$ and $P_{11}(1840)$ resonances. To achieve a good description of the recent C_x and C_z CLAS measurements, the $P_{13}(1900)$ had to be introduced. It should be noted that, at this stage of the analysis, the contribution of the missing $D_{13}(1900)$ is significantly reduced as compared to previous versions of the model. As shown in figs. 9-11, this last version (solid line) provides a good overall agreement. On the contrary, the solution without the $P_{13}(1900)$ (not shown) fails to reproduce the data.

More refined analyses with the RPR and BG models are in progress and will be published later on. Comparison with the dynamical coupled-channel model of Saclay-Argonne-Pittsburgh [25]-[27] has also started.

5 Summary

In this paper, we have presented new results for the reaction $\gamma p \rightarrow K^+ \Lambda$ from threshold to $E_\gamma \sim 1500$ MeV. Measurements of the beam-recoil observables O_x , O_z and target asymmetries T were obtained over a wide angular range. We have compared our results with two isobar models which are in reasonable agreement with the whole data set. They both confirm the necessity to introduce new or poorly known resonances in the 1900 MeV mass region (P_{13} and/or D_{13}).

It should be underlined that from now on only one additional double polarization observable (beam-target or target-recoil) would be sufficient to extract the four helicity amplitudes of the reaction.

Acknowledgements

We are grateful to A.V. Sarantsev, B. Saghai, T. Corthals, J. Ryckebusch and P. Vancraeyveld for communication of their most recent analyses and J.M. Richard for fruitful discussions on the spin observable constraints. We thank R. Schumacher for communication of the CLAS data. The support of the technical groups from all contributing institutions is greatly acknowledged. It is a pleasure to thank the ESRF as a host institution and its technical staff for the smooth operation of the storage ring.

References

1. R.K.Bradford *et al.*, Phys. Rev. C **73**, 035202 (2006).
2. K.-H. Glander *et al.*, Eur. Phys. J. A **19**, 251 (2004).
3. J.W.C. McNabb *et al.*, Phys. Rev. C **69**, 042201(R) (2004).
4. M. Sumihama *et al.*, Phys. Rev. C **73**, 035214 (2006).
5. A. Lleres *et al.*, Eur. Phys. J. A **31**, 79 (2007).
6. R.G.T. Zegers *et al.*, Phys. Rev. Lett. **91**, 092001 (2003).
7. R.K.Bradford *et al.*, Phys. Rev. C **75**, 035205 (2007).
8. O. Bartalini *et al.*, Eur. Phys. J. A **26**, 399 (2005).
9. *Review of Particle Physics 2004*, Phys. Lett. B **592**, 1 (2004).
10. R.A. Adelseck and B. Saghai, Phys. Rev. C **42**, 108 (1990).
11. I.S. Barker, A. Donnachie and J.K. Storrow, Nucl. Phys. B **95**, 347 (1975).
12. P. Calvat, Thesis, Université J. Fourier Grenoble, 1997, unpublished.
13. T.D. Lee and C.N. Yang, Phys. Rev. **108**, 1645 (1957).
14. W.T. Chiang and F. Tabakin, Phys. Rev. C **55**, 2054 (1997).
15. X. Artru, J.M. Richard and J. Soffer, Phys. Rev. C **75**, 024002 (2007).
16. T. Corthals, J. Ryckebusch and T. Van Cauteren, Phys. Rev. C **73**, 045207 (2006).
17. T. Corthals, Thesis, Universiteit Gent, 2007, unpublished.
18. T. Corthals *et al.*, Phys. Lett. B **656**, 186 (2007).
19. T. Corthals, J. Ryckebusch and P. Vancraeyveld, private communication.
20. A.V. Anisovich *et al.*, Eur. Phys. J. A **25**, 427 (2005).
21. A.V. Sarantsev *et al.*, Eur. Phys. J. A **25**, 441 (2005).
22. A.V. Anisovich *et al.*, Eur. Phys. J. A **34**, 243 (2007).
23. V.A. Nikonov *et al.*, arXiv:hep-ph/0707.3600 (2007).
24. A. Sarantsev, private communication.
25. B. Juliá-Díaz, B. Saghai, T.-S.H. Lee and F. Tabakin, Phys. Rev. C **73**, 055204 (2006).
26. B. Saghai, J.C. David, B. Juliá-Díaz and T.-S.H. Lee, Eur. Phys. J. A **31**, 512 (2007).
27. B. Saghai, private communication.

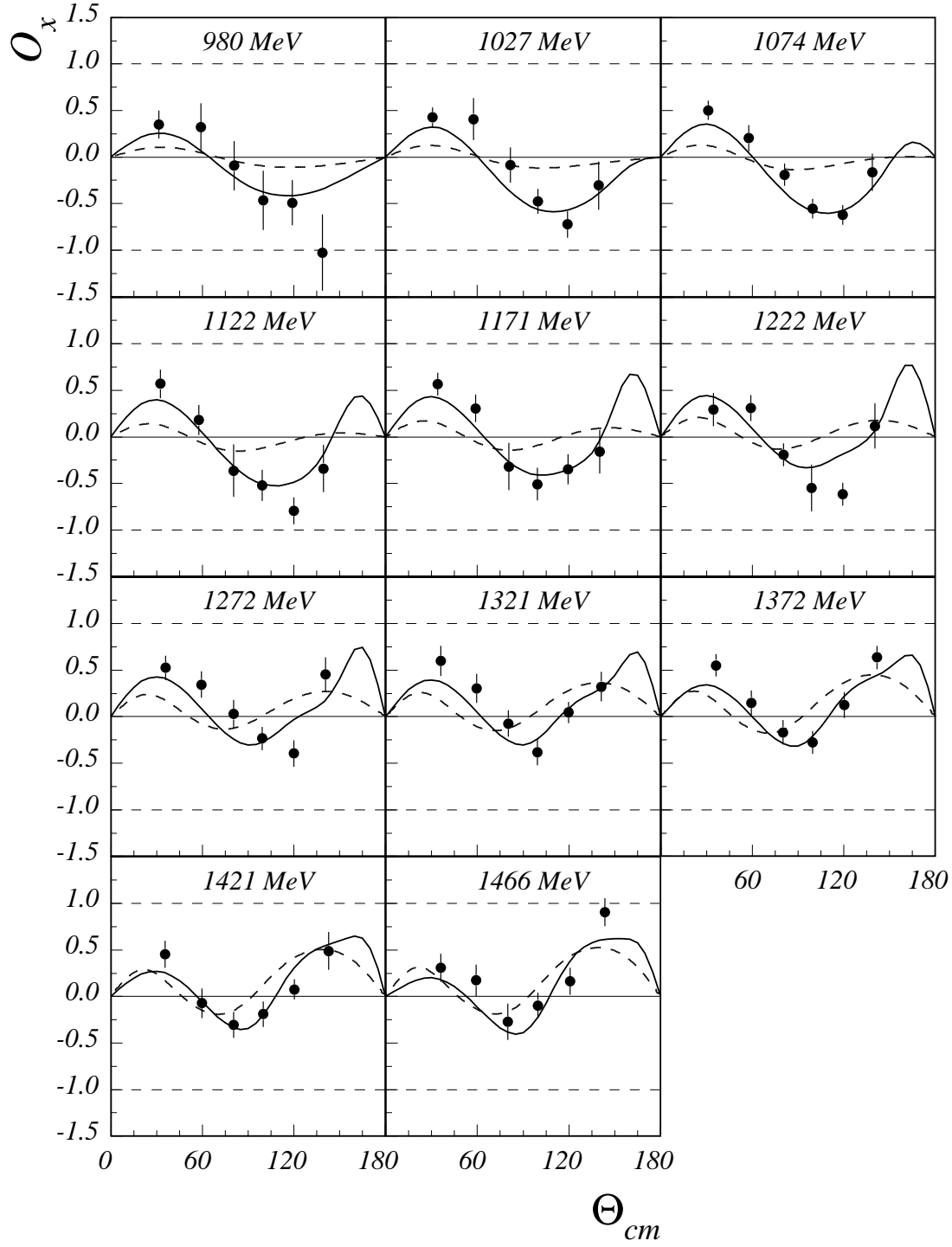


Fig. 9. Angular distributions of the beam recoil observable O_x . Data are compared with the predictions of the BG (solid line) and RPR (dashed line) models.

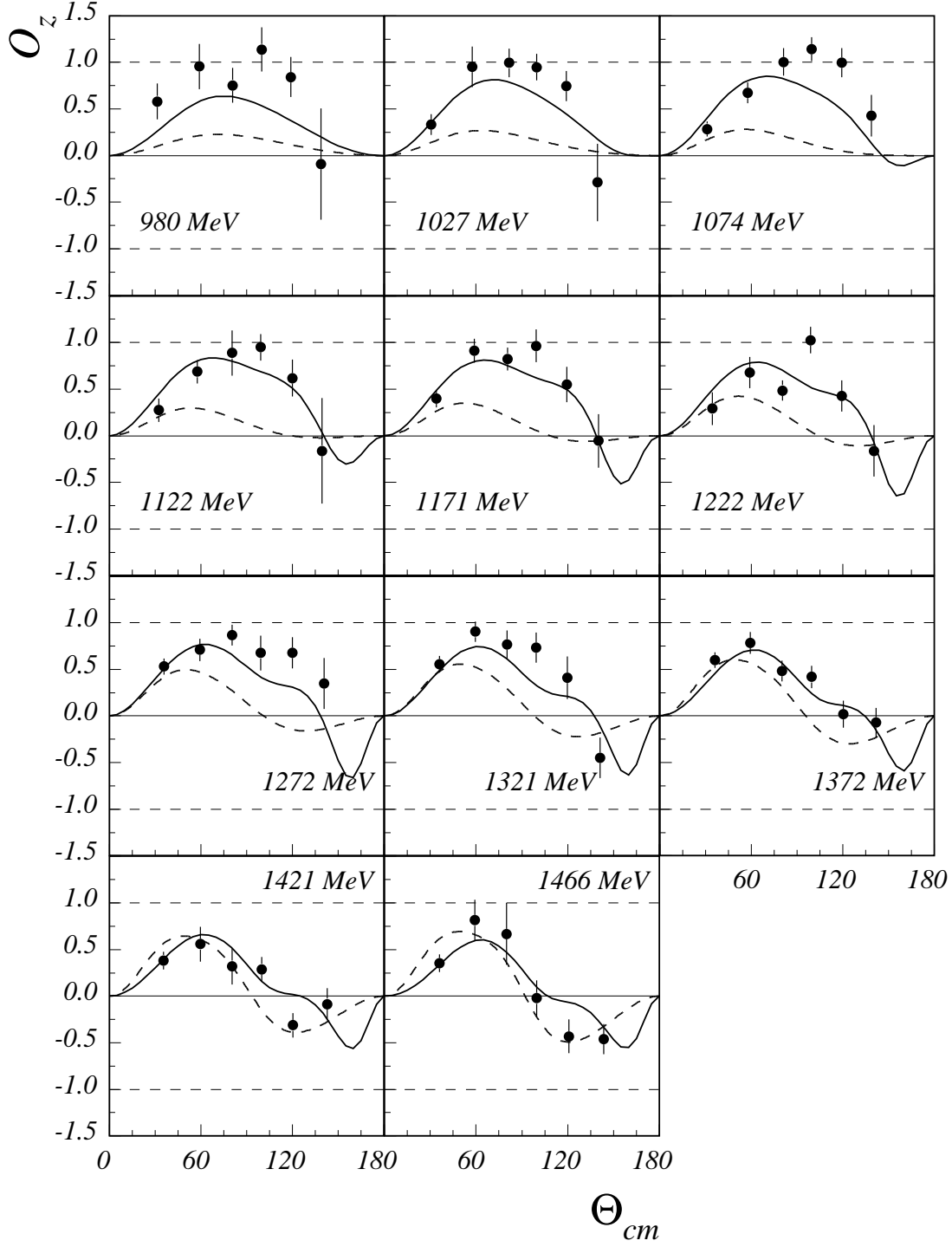


Fig. 10. Angular distributions of the beam recoil observable O_z . Data are compared with the predictions of the BG (solid line) and RPR (dashed line) models.

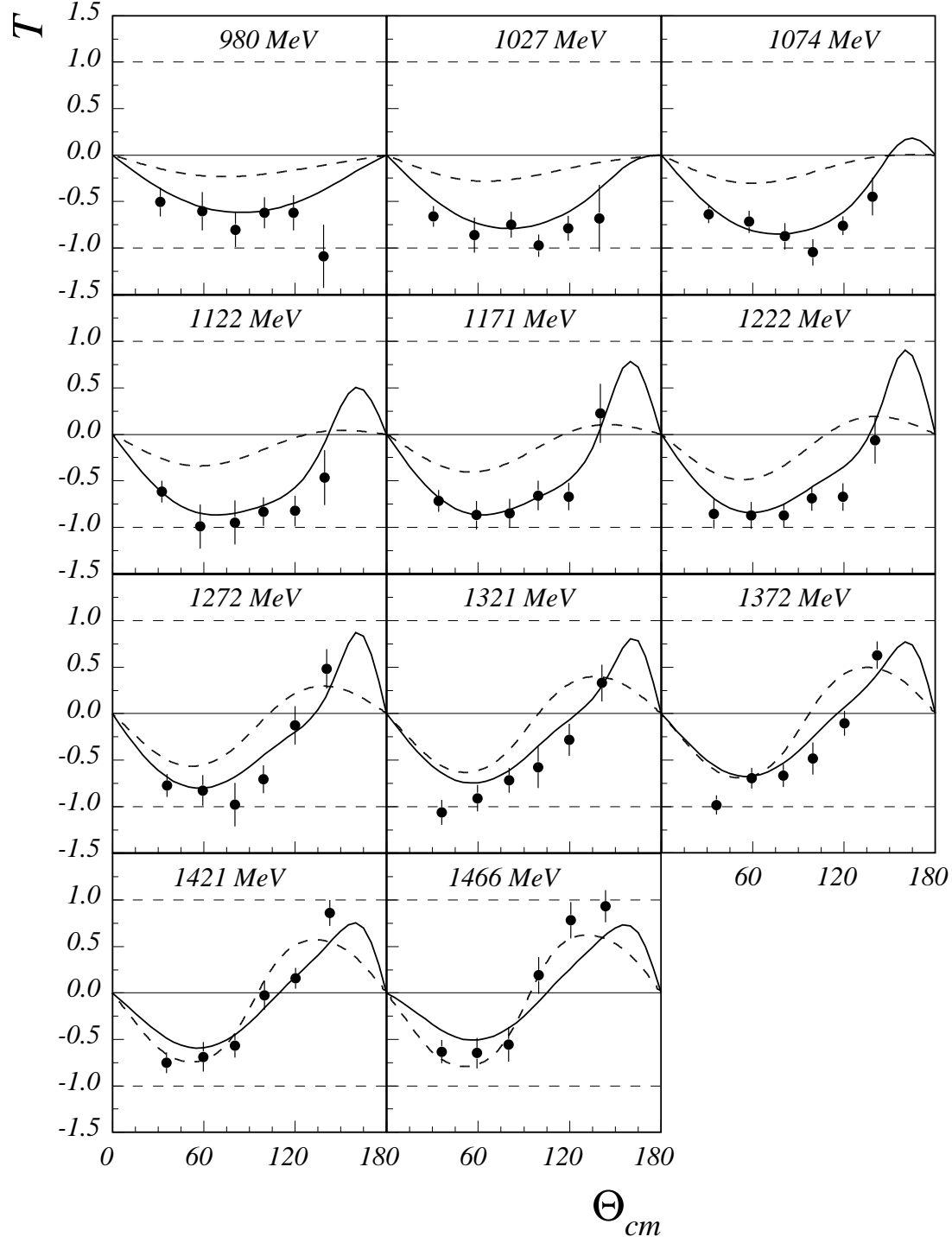


Fig. 11. Angular distributions of the target asymmetry T . Data are compared with the predictions of the BG (solid line) and RPR (dashed line) models.

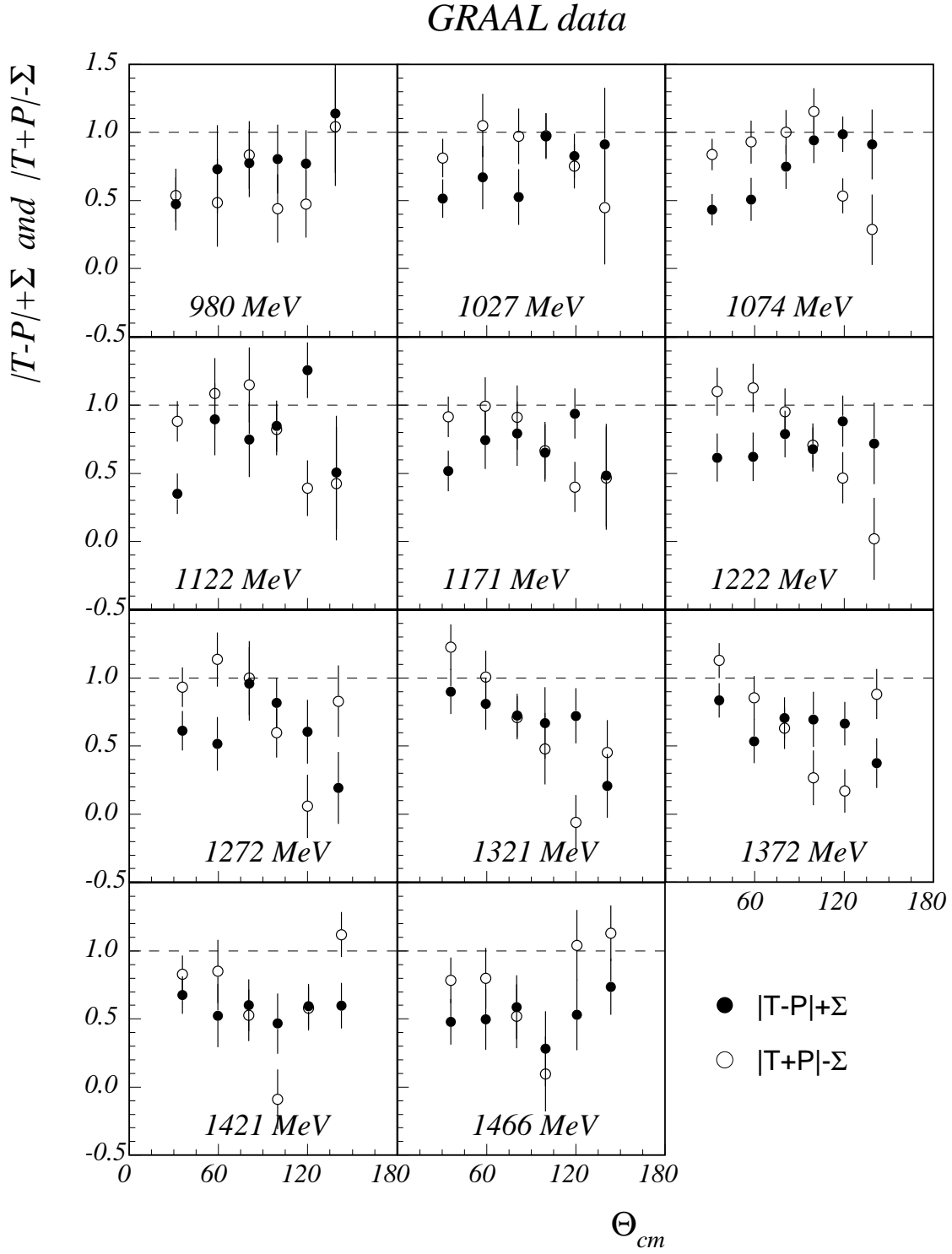


Fig. 12. Angular distributions of the quantities $|T - P| + \Sigma$ (closed circles) and $|T + P| - \Sigma$ (open circles). We should have the inequalities $|T \pm P| \mp \Sigma \leq 1$ (eq. 33).

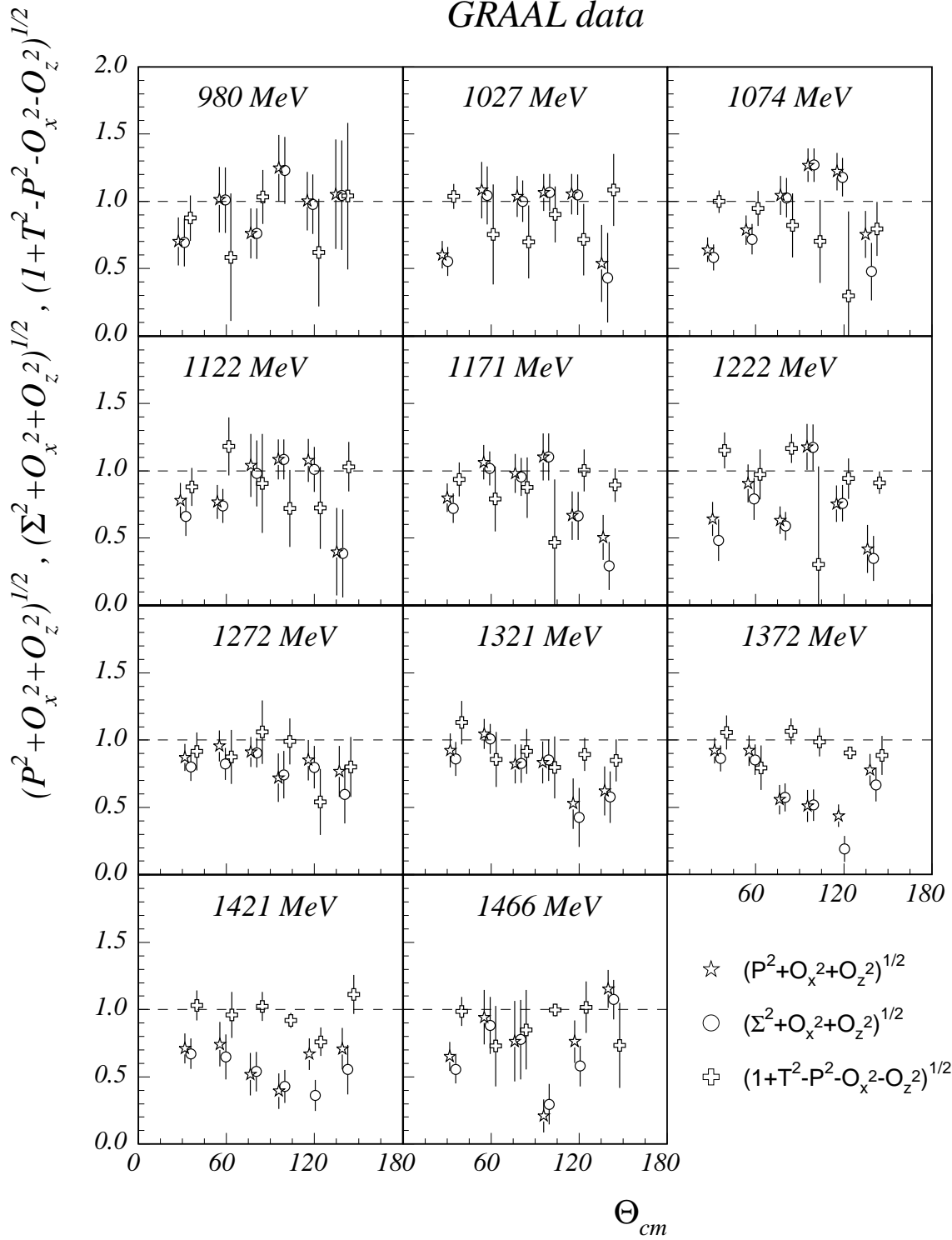


Fig. 13. Angular distributions of the quantities $(P^2 + O_x^2 + O_z^2)^{1/2}$ (stars), $(\Sigma^2 + O_x^2 + O_z^2)^{1/2}$ (circles) and $(1 + T^2 - P^2 - O_x^2 - O_z^2)^{1/2} = (\Sigma^2 + C_x^2 + C_z^2)^{1/2}$ (crosses). The first and third sets of data are horizontally shifted for visualization. All these quantities should be ≤ 1 (inequalities 34, 35 and 37).

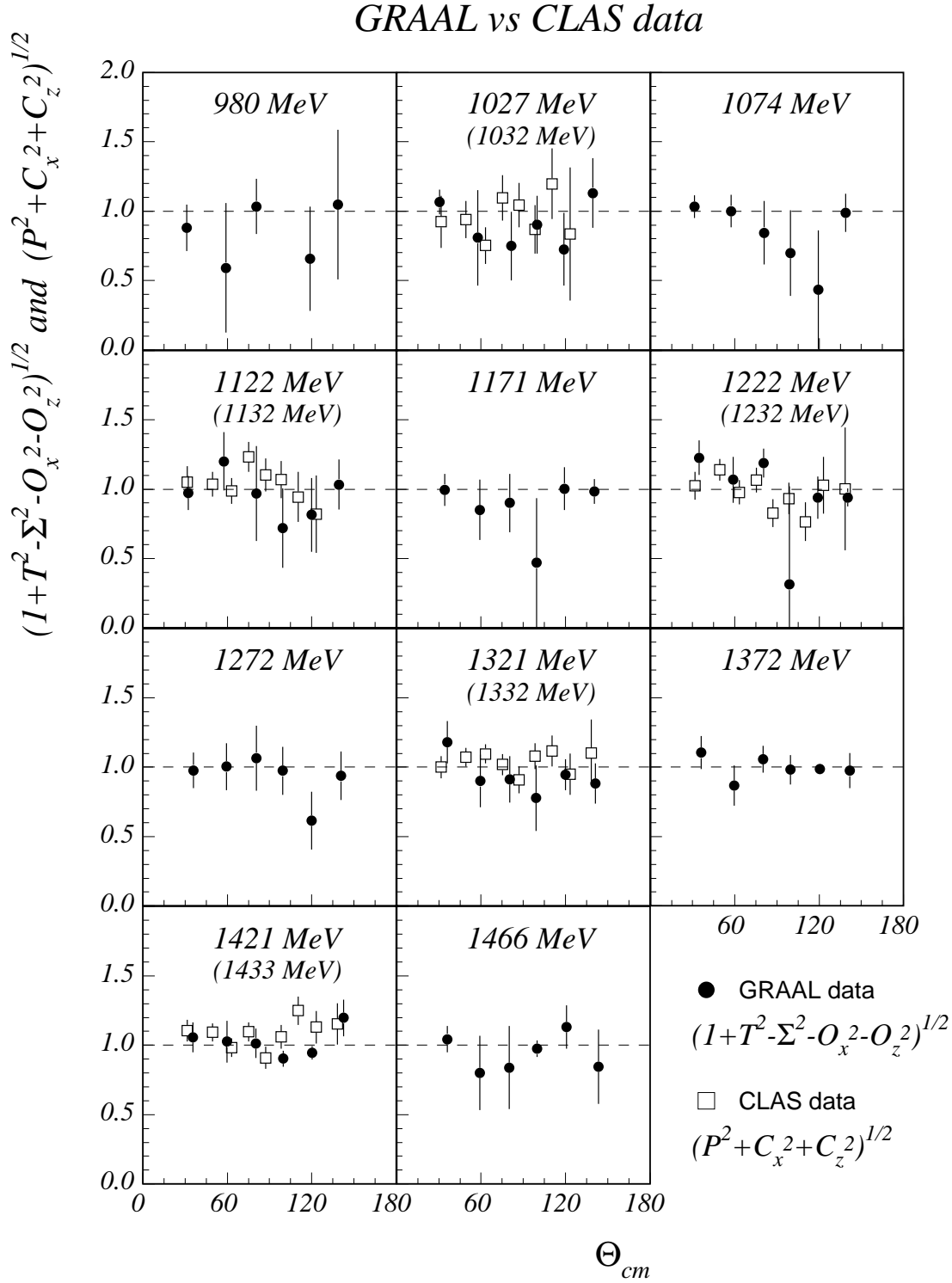


Fig. 14. Angular distributions of the quantity $(1 + T^2 - \Sigma^2 - O_x^2 - O_z^2)^{1/2} = (P^2 + C_x^2 + C_z^2)^{1/2}$. This quantity should be ≤ 1 (inequality 36). Comparison to the values $(P^2 + C_x^2 + C_z^2)^{1/2}$ published by the CLAS collaboration (open squares - energy in parentheses). Note that the $O_x^2 + O_z^2$ and $C_x^2 + C_z^2$ values are independent of the choice for the axes specifying the Λ polarization (see sect. 3.2.1).

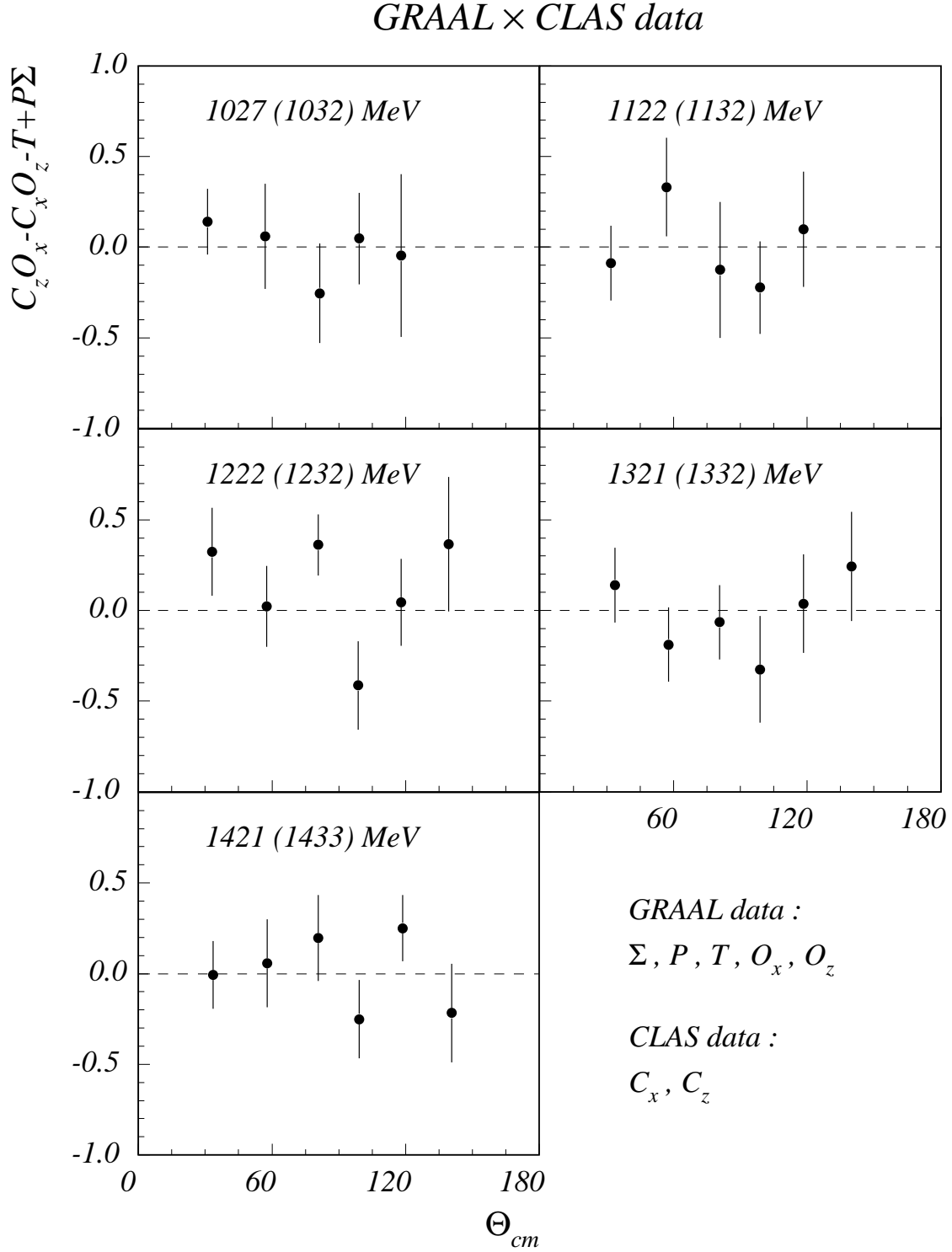


Fig. 15. Angular distributions of the quantity $C_z O_x - C_x O_z - T + P \Sigma$. This quantity is calculated using the C_x and C_z results published by the CLAS collaboration (energy in parentheses) combined with our O_x and O_z data converted by eq. 2 to have the same \hat{z}' axis convention and with our Σ , P and T measurements. The used CLAS data are those corresponding to the angles $\cos \theta_{cm} = 0.85$, $\text{mean}(0.65, 0.45)$, $\text{mean}(0.25, 0.05)$, -0.15 , $\text{mean}(-0.35, -0.55)$ and -0.75 . We should have the equality $C_z O_x - C_x O_z - T + P \Sigma = 0$ (eq. 32).

Table 1. Beam-recoil O_x values.

$\theta_{cm}(^\circ)$	$E_\gamma=980$ MeV	$\theta_{cm}(^\circ)$	$E_\gamma=1027$ MeV	$\theta_{cm}(^\circ)$	$E_\gamma=1074$ MeV	$\theta_{cm}(^\circ)$	$E_\gamma=1122$ MeV
31.3	0.349 ± 0.150	30.6	0.425 ± 0.108	31.2	0.502 ± 0.103	32.4	0.570 ± 0.154
59.1	0.320 ± 0.255	57.5	0.408 ± 0.225	57.5	0.202 ± 0.140	57.6	0.179 ± 0.161
80.7	-0.094 ± 0.262	81.7	-0.085 ± 0.189	81.0	-0.190 ± 0.120	80.6	-0.365 ± 0.282
99.8	-0.464 ± 0.320	99.8	-0.477 ± 0.133	99.7	-0.552 ± 0.106	99.2	-0.522 ± 0.165
118.9	-0.490 ± 0.244	119.0	-0.723 ± 0.142	119.3	-0.621 ± 0.105	119.9	-0.795 ± 0.146
138.6	-1.028 ± 0.410	139.5	-0.304 ± 0.259	138.8	-0.163 ± 0.200	139.3	-0.341 ± 0.252
$\theta_{cm}(^\circ)$	$E_\gamma=1171$ MeV	$\theta_{cm}(^\circ)$	$E_\gamma=1222$ MeV	$\theta_{cm}(^\circ)$	$E_\gamma=1272$ MeV	$\theta_{cm}(^\circ)$	$E_\gamma=1321$ MeV
34.1	0.567 ± 0.122	34.6	0.294 ± 0.179	35.8	0.526 ± 0.130	36.0	0.599 ± 0.161
58.9	0.306 ± 0.148	58.9	0.310 ± 0.139	59.2	0.345 ± 0.140	59.4	0.304 ± 0.155
80.5	-0.319 ± 0.254	80.4	-0.193 ± 0.124	80.6	0.028 ± 0.155	80.3	-0.073 ± 0.142
99.3	-0.510 ± 0.175	98.9	-0.548 ± 0.252	99.2	-0.232 ± 0.125	99.2	-0.383 ± 0.141
119.4	-0.347 ± 0.162	119.1	-0.615 ± 0.121	119.9	-0.395 ± 0.143	119.9	0.046 ± 0.114
140.4	-0.160 ± 0.234	140.3	0.116 ± 0.242	140.8	0.454 ± 0.187	141.3	0.323 ± 0.158
$\theta_{cm}(^\circ)$	$E_\gamma=1372$ MeV	$\theta_{cm}(^\circ)$	$E_\gamma=1421$ MeV	$\theta_{cm}(^\circ)$	$E_\gamma=1466$ MeV		
36.1	0.552 ± 0.119	35.7	0.455 ± 0.144	35.9	0.307 ± 0.150		
59.5	0.150 ± 0.130	59.6	-0.072 ± 0.160	59.3	0.172 ± 0.171		
80.1	-0.168 ± 0.131	80.3	-0.303 ± 0.139	80.0	-0.270 ± 0.195		
99.4	-0.276 ± 0.122	99.7	-0.190 ± 0.137	99.7	-0.096 ± 0.139		
120.4	0.124 ± 0.138	120.4	0.076 ± 0.110	120.8	0.164 ± 0.145		
141.9	0.636 ± 0.126	142.8	0.490 ± 0.205	143.7	0.905 ± 0.152		

Table 2. Beam-recoil O_z values.

$\theta_{cm}(^\circ)$	$E_\gamma=980$ MeV	$\theta_{cm}(^\circ)$	$E_\gamma=1027$ MeV	$\theta_{cm}(^\circ)$	$E_\gamma=1074$ MeV	$\theta_{cm}(^\circ)$	$E_\gamma=1122$ MeV
31.3	0.581 ± 0.194	30.6	0.333 ± 0.110	31.2	0.285 ± 0.080	32.4	0.274 ± 0.124
59.1	0.956 ± 0.242	57.5	0.951 ± 0.216	57.5	0.674 ± 0.112	57.6	0.687 ± 0.127
80.7	0.754 ± 0.186	81.7	0.995 ± 0.154	81.0	1.003 ± 0.148	80.6	0.888 ± 0.244
99.8	1.139 ± 0.237	99.8	0.949 ± 0.140	99.7	1.140 ± 0.130	99.2	0.950 ± 0.144
118.9	0.841 ± 0.215	119.0	0.744 ± 0.162	119.3	0.996 ± 0.156	119.9	0.618 ± 0.197
138.6	-0.091 ± 0.597	139.5	-0.287 ± 0.415	138.8	0.427 ± 0.223	139.3	-0.162 ± 0.568
$\theta_{cm}(^\circ)$	$E_\gamma=1171$ MeV	$\theta_{cm}(^\circ)$	$E_\gamma=1222$ MeV	$\theta_{cm}(^\circ)$	$E_\gamma=1272$ MeV	$\theta_{cm}(^\circ)$	$E_\gamma=1321$ MeV
34.1	0.398 ± 0.093	34.6	0.291 ± 0.177	35.8	0.532 ± 0.087	36.0	0.554 ± 0.090
58.9	0.914 ± 0.128	58.9	0.678 ± 0.167	59.2	0.710 ± 0.119	59.4	0.904 ± 0.108
80.5	0.825 ± 0.123	80.4	0.485 ± 0.109	80.6	0.867 ± 0.112	80.3	0.767 ± 0.153
99.3	0.964 ± 0.175	98.9	1.025 ± 0.143	99.2	0.676 ± 0.188	99.2	0.734 ± 0.161
119.4	0.550 ± 0.190	119.1	0.426 ± 0.166	119.9	0.677 ± 0.166	119.9	0.409 ± 0.229
140.4	-0.055 ± 0.286	140.3	-0.162 ± 0.276	140.8	0.349 ± 0.272	141.3	-0.448 ± 0.217
$\theta_{cm}(^\circ)$	$E_\gamma=1372$ MeV	$\theta_{cm}(^\circ)$	$E_\gamma=1421$ MeV	$\theta_{cm}(^\circ)$	$E_\gamma=1466$ MeV		
36.1	0.600 ± 0.084	35.7	0.384 ± 0.094	35.9	0.354 ± 0.095		
59.4	0.784 ± 0.119	59.6	0.558 ± 0.185	59.3	0.814 ± 0.222		
80.1	0.484 ± 0.112	80.3	0.322 ± 0.195	80.0	0.666 ± 0.332		
99.4	0.419 ± 0.120	99.7	0.289 ± 0.134	99.7	-0.023 ± 0.192		
120.4	0.019 ± 0.145	120.4	-0.313 ± 0.131	120.8	-0.432 ± 0.180		
141.9	-0.072 ± 0.159	142.8	-0.085 ± 0.172	143.7	-0.461 ± 0.162		

Table 3. Target asymmetry T values.

$\theta_{cm}(^{\circ})$	$E_{\gamma}=980$ MeV	$\theta_{cm}(^{\circ})$	$E_{\gamma}=1027$ MeV	$\theta_{cm}(^{\circ})$	$E_{\gamma}=1074$ MeV	$\theta_{cm}(^{\circ})$	$E_{\gamma}=1122$ MeV
31.3	-0.506 ± 0.156	30.6	-0.663 ± 0.112	31.2	-0.635 ± 0.096	32.4	-0.615 ± 0.118
59.1	-0.607 ± 0.206	57.5	-0.860 ± 0.190	57.5	-0.718 ± 0.120	57.6	-0.991 ± 0.237
80.7	-0.803 ± 0.185	81.7	-0.749 ± 0.139	81.0	-0.874 ± 0.141	80.6	-0.949 ± 0.239
99.8	-0.622 ± 0.166	99.8	-0.974 ± 0.121	99.7	-1.048 ± 0.140	99.2	-0.833 ± 0.153
118.9	-0.622 ± 0.187	119.0	-0.789 ± 0.133	119.3	-0.760 ± 0.102	119.9	-0.825 ± 0.165
138.6	-1.090 ± 0.341	139.5	-0.681 ± 0.359	138.8	-0.448 ± 0.203	139.3	-0.465 ± 0.296
$\theta_{cm}(^{\circ})$	$E_{\gamma}=1171$ MeV	$\theta_{cm}(^{\circ})$	$E_{\gamma}=1222$ MeV	$\theta_{cm}(^{\circ})$	$E_{\gamma}=1272$ MeV	$\theta_{cm}(^{\circ})$	$E_{\gamma}=1321$ MeV
34.1	-0.715 ± 0.116	34.6	-0.858 ± 0.155	35.8	-0.773 ± 0.123	36.0	-1.064 ± 0.133
58.9	-0.869 ± 0.154	58.9	-0.874 ± 0.145	59.2	-0.827 ± 0.166	59.4	-0.910 ± 0.142
80.5	-0.850 ± 0.158	80.4	-0.871 ± 0.124	80.6	-0.979 ± 0.234	80.3	-0.716 ± 0.133
99.3	-0.659 ± 0.159	98.9	-0.690 ± 0.132	99.2	-0.707 ± 0.150	99.2	-0.576 ± 0.223
119.4	-0.669 ± 0.150	119.1	-0.675 ± 0.145	119.9	-0.125 ± 0.208	119.9	-0.281 ± 0.174
140.4	0.226 ± 0.316	140.3	-0.066 ± 0.249	140.8	0.482 ± 0.213	141.3	0.331 ± 0.198
$\theta_{cm}(^{\circ})$	$E_{\gamma}=1372$ MeV	$\theta_{cm}(^{\circ})$	$E_{\gamma}=1421$ MeV	$\theta_{cm}(^{\circ})$	$E_{\gamma}=1466$ MeV		
36.1	-0.983 ± 0.104	35.7	-0.753 ± 0.112	35.9	-0.632 ± 0.127		
59.5	-0.695 ± 0.113	59.6	-0.687 ± 0.159	59.3	-0.648 ± 0.166		
80.1	-0.669 ± 0.123	80.3	-0.564 ± 0.131	80.0	-0.553 ± 0.185		
99.4	-0.482 ± 0.175	99.7	-0.025 ± 0.157	99.7	0.190 ± 0.196		
120.4	-0.104 ± 0.135	120.4	0.160 ± 0.112	120.8	0.785 ± 0.195		
141.9	0.629 ± 0.147	142.8	0.859 ± 0.140	143.7	0.933 ± 0.175		